

## Article

# The Effect of Intraocular Pressure Load Boundary on the Biomechanics of the Human Conventional Aqueous Outflow Pathway

Alireza Karimi <sup>1,\*</sup>, Reza Razaghi <sup>1</sup>, Seyed Mohammadali Rahmati <sup>2</sup>, J. Crawford Downs <sup>1</sup>, Ted S. Acott <sup>3</sup>, Mary J. Kelley <sup>4</sup>, Ruikang K. Wang <sup>5,6</sup> and Murray Johnstone <sup>5</sup>

<sup>1</sup> Department of Ophthalmology and Visual Sciences, University of Alabama at Birmingham, Birmingham, AL 35233, USA

<sup>2</sup> School of Biological Sciences, Georgia Institute of Technology, Atlanta, GA 30332, USA

<sup>3</sup> Departments of Ophthalmology and Biochemistry and Molecular Biology, Casey Eye Institute, Oregon Health & Science University, Portland, OR 97239, USA

<sup>4</sup> Departments of Ophthalmology and Integrative Biosciences, Casey Eye Institute, Oregon Health & Science University, Portland, OR 97239, USA

<sup>5</sup> Department of Ophthalmology, University of Washington, Seattle, WA 98195, USA

<sup>6</sup> Department of Bioengineering, University of Washington, Seattle, WA 98195, USA

\* Correspondence: akarimi@uabmc.edu



**Citation:** Karimi, A.; Razaghi, R.; Rahmati, S.M.; Downs, J.C.; Acott, T.S.; Kelley, M.J.; Wang, R.K.; Johnstone, M. The Effect of Intraocular Pressure Load Boundary on the Biomechanics of the Human Conventional Aqueous Outflow Pathway. *Bioengineering* **2022**, *9*, 672. <https://doi.org/10.3390/bioengineering9110672>

Academic Editor: Kwong Ming Tse

Received: 25 September 2022

Accepted: 8 November 2022

Published: 10 November 2022

**Publisher's Note:** MDPI stays neutral with regard to jurisdictional claims in published maps and institutional affiliations.



**Copyright:** © 2022 by the authors. Licensee MDPI, Basel, Switzerland. This article is an open access article distributed under the terms and conditions of the Creative Commons Attribution (CC BY) license (<https://creativecommons.org/licenses/by/4.0/>).

**Abstract:** Background: Aqueous humor outflow resistance in the trabecular meshwork (TM), juxtacanalicular connective tissue (JCT), and Schlemm's canal (SC) endothelium of the conventional outflow pathway actively contribute to intraocular pressure (IOP) regulation. Outflow resistance is actively affected by the dynamic outflow pressure gradient across the TM, JCT, and SC inner wall tissues. The resistance effect implies the presence of a fluid–structure interaction (FSI) coupling between the outflow tissues and the aqueous humor. However, the biomechanical interactions between viscoelastic outflow tissues and aqueous humor dynamics are largely unknown. Methods: A 3D microstructural finite element (FE) model of a healthy human eye TM/JCT/SC complex was constructed with elastic and viscoelastic material properties for the bulk extracellular matrix and embedded elastic cable elements. The FE models were subjected to both idealized and a physiologic IOP load boundary using the FSI method. Results: The elastic material model for both the idealized and physiologic IOP load boundary at equal IOPs showed similar stresses and strains in the outflow tissues as well as pressure in the aqueous humor. However, outflow tissues with viscoelastic material properties were sensitive to the IOP load rate, resulting in different mechanical and hydrodynamic responses in the tissues and aqueous humor. Conclusions: Transient IOP fluctuations may cause a relatively large IOP difference of ~20 mmHg in a very short time frame of ~0.1 s, resulting in a rate stiffening in the outflow tissues. Rate stiffening reduces strains and causes a rate-dependent pressure gradient across the outflow tissues. Thus, the results suggest it is necessary to use a viscoelastic material model in outflow tissues that includes the important role of IOP load rate.

**Keywords:** trabecular meshwork; juxtacanalicular tissue; Schlemm's canal; viscoelastic material model; transient IOP fluctuations; fluid–structure interaction

## 1. Introduction

The aqueous humor outflow resistance in the conventional outflow pathway is the primary determinant of intraocular pressure (IOP) [1–4]. Dysregulation in the balance between the aqueous inflow and outflow can result in an IOP elevation that is associated with primary open-angle glaucoma (POAG) [5–12]. Aqueous humor passes through the trabecular meshwork (TM) and the juxtacanalicular connective tissue (JCT). After crossing the TM, JCT, and inner wall endothelium of Schlemm's canal (SC), aqueous humor enters

the SC lumen and eventually flows circumferentially to the collector channels leading to the aqueous and episcleral veins [13–17].

Transient IOP fluctuations [12,18–24] result in a dynamic mechanical environment in the outflow pathway that actively affects the geometry and cellular mechanotransduction of the outflow tissues [25–27] as well as the outflow resistance [28]. Active outflow resistance regulation in the conventional outflow pathway results in a dynamic outflow pressure gradient across the outflow tissues [9,29,30]. The TM responds mechanically to IOP fluctuations by undergoing geometric changes, resulting in an interaction between the outflow tissues and aqueous humor [29]. Cell and tissue constituents of the TM, JCT, and SC respond to the pressure gradient by adjusting the tissue and cellular elasticity [17]. Thus, TM/JCT/SC motion and its resulting mechanisms of aqueous outflow resistance [31,32] mainly depend on the biomechanical properties of outflow tissues [33–36]. The pulsatile motion of the TM reflects the tissue's deformability in response to the cardiac-induced ocular pulse amplitude [37], and the TM's stiffness is a key parameter in determining TM pulsatile motion [38]. It has been shown that the TM experiences different displacements with IOP fluctuation [31,32] that demonstrate the viscoelasticity of the TM tissue. However, one may argue that these displacements in the TM relate to the ocular pulse since a significant correlation has been reported between the TM displacement and ocular pulse amplitude [31]. However, Li and colleagues used phase-sensitive optical coherence tomography (PhS-OCT) to show that TM displacement is strongly IOP load rate-dependent at a constant ocular pulse amplitude in ex vivo nonhuman primate eyes (*Macaca nemestrina*). Thus, as load rate increases, the same IOP pulse amplitude results in progressively smaller displacements of the TM [33], indicating that the TM is viscoelastic.

To date, experimental [38–40] and numerical [40,41] TM biomechanics studies have been limited to using isotropic elastic and hyperelastic mechanical properties to model the TM, and yet soft biological tissues are generally both anisotropic and viscoelastic [42–47]. Elastic materials restore the specimen to its initial configuration by releasing stored energy from loading. In contrast, viscoelastic materials dissipate some stored energy [48], causing a load rate-dependent mechanical response. IOP causes microscopic mechanical deformations in the extracellular matrix of the TM, JCT, and SC inner wall tissues [27,49–51]. Soft biological tissues such as those in the outflow pathway are typically viscoelastic and their mechanical responses depend on the load rate. Therefore, it is reasonable to speculate that the outflow pressure gradient across the TM/JCT/SC inner wall complex depends on the rate of change in IOP (load), which may result in dynamic changes in outflow resistance. However, the dynamics of aqueous humor interactions with the local and global biomechanical responses of the outflow pathway tissues are largely unknown.

Karimi and colleagues recently calculated the viscoelastic mechanical properties of the TM/JCT/SC complex [52] using a finite element (FE)-optimization method and dynamic SC pressurization experimental setup [53]. We showed that the elastic material model was unable to capture the time-dependent mechanical response of the outflow tissues. In contrast, the viscoelastic material model successfully captured the tissues' dynamic motion and resulted in a good match with spectral domain PhS-OCT imaging data [53]. Applying the viscoelastic material model allows us to include the important effect of dynamic IOP changes across the outflow pathway. The model can then simultaneously assess the hydrodynamics and the resultant stresses and strains of the outflow tissues [48,54–56]. The findings may significantly enhance the accuracy of the modeling results. It is suggested that there must be an active fluid–structure interaction (FSI) providing coupling between the outflow tissues and outflow resistance that actively contributes to IOP regulation [57,58]. Experimental studies also showed a significant correlation between cyclic responses that affect the biomechanics of the outflow tissues and the resultant balance of aqueous inflow and outflow [59]. Doubling the inflow rate resulted in an immediate ~2-fold IOP elevation, which returned to baseline regulation after several days of continued perfusion [57].

Karimi [60] recently developed a 3D FSI microstructural model of a healthy human conventional outflow pathway. We showed a larger aqueous humor pressure drop across

the outflow pathway with stiffer tissues. However, we used a simple elastic material model with an idealized IOP load boundary that may not fully represent the dynamic biomechanical behavior seen with a physiologic load boundary. While great strides have been made in understanding the mechanisms that regulate aqueous outflow resistance in the conventional outflow pathway [3,4,28,58,61–65], the mechanism of outflow resistance regulation with a dynamic physiologic IOP load boundary is largely unknown. Although it has been shown experimentally [38,66] and numerically [60] that increased TM stiffness causes increased outflow resistance, it remains unclear how viscoelastic outflow tissues with a physiologic IOP load boundary may affect outflow resistance. To date, clinical and experimental techniques have been unable to quantify the biomechanical stresses and strains in the outflow tissues considering their time-dependent mechanical properties and transient IOP fluctuations. Numerical approaches, such as the FSI, allow us to calculate the local resultant stresses and strains across the TM, JCT, and SC inner wall tissues, as well as hydrodynamics of the aqueous humor. FSI studies can estimate the regions with relatively higher shear stresses that are thought to play an important role in IOP regulation through the endothelial nitric oxide pathway [67–69] and include the biomechanical interaction of aqueous humor with the deformable tissue walls that can advance our understanding of IOP regulation [19,27,53,60]. We can thereby conceptualize new approaches for diagnostic and therapeutic methods to cope with ocular hypertension and glaucoma [31].

In this study, we constructed a microstructural TM/JCT/SC complex FE model of a normal human eye [60] using the elastic and viscoelastic extracellular matrix of the outflow tissues with embedded elastic cable elements that represent the directional stiffness imparted by anisotropic collagen fibrils [53]. The tissues were subjected to an idealized and physiologic IOP load boundary by means of controlling steady state or pulsatile aqueous humor inflow. The resultant stresses and strains in the outflow tissues and hydrodynamics in the aqueous humor were calculated using the FSI method, and results were compared.

## 2. Materials and Methods

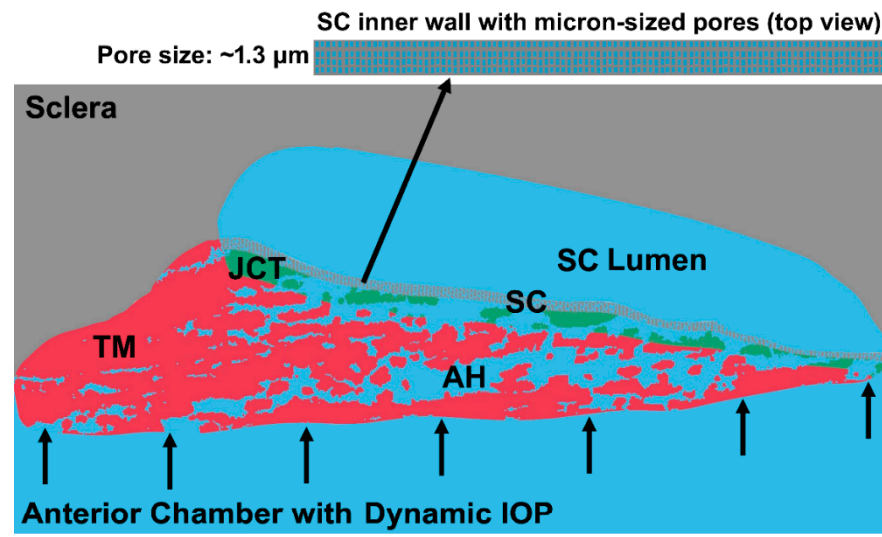
### 2.1. Human Eye Imaging, FE Reconstruction, Cable Elements Distribution, Material Models, Hydraulic Conductivity, and Boundary Conditions

The FE model of the TM/JCT/SC complex consisting of the sclera, outflow system, and cornea was obtained as described in our prior publication [70]. The imaging, segmentation, and volume meshing methods of the TM/JCT/SC complex FE model were fully explained in our prior publications [53,60]. A wedge of the anterior segment was imaged and [71] volume meshed [70,72]. The model [73] was separated into the TM with adjacent JCT (~10  $\mu\text{m}$  [71]) and SC inner wall (~5  $\mu\text{m}$  [30]) regions as shown in Figure 1. Idealized  $\mu\text{m}$ -sized pores were distributed in the SC inner wall [74] with a pore density and diameter of 835 pores/ $\text{mm}^2$  [30] and 1.3  $\mu\text{m}$  [75], respectively (Figure 1a inset). Element quality assessment was conducted using Ansys (Ansys Inc., Pittsburgh, PA, USA) [52,73,76–78] to make sure the Jacobian ratio, aspect ratio, warping factor, and skewness were within the acceptable ranges for a good quality element (Ansys Inc.). Mesh density analyses were performed for the FE model described in our prior publications [53,60].

The cable elements were distributed in the extracellular matrix of the TM and JCT (Figure 1b) using a mesh-free, penalty-based, cable-in-solid coupling algorithm [52] to represent the directional stiffness imparted by anisotropic collagen fibril orientation in those tissues [17,79–86]. The cable elements were modeled with an elastic material, and the extracellular matrix was modeled with elastic and viscoelastic materials using 8-noded hexahedral solid elements with a fully integrated element formulation [87]. The elastic modulus of the sclera was 2.93 MPa [88] and nearly incompressible (Poisson's ratio,  $\nu = 0.495$ ) [89,90]. The elastic modulus of the TM/JCT/SC complex was 0.148 MPa, nearly incompressible (Poisson's ratio,  $\nu = 0.495$ ), with the cable element elastic modulus of 1280 MPa as calculated in our prior publication using an FE-optimization algorithm matched with spectral domain PhS-OCT imaging data [53]. In the viscoelastic model, the material parameters

were  $G_0$  (short-time shear modulus) = 6.36 MPa,  $G_\infty$  (long-time shear modulus) = 1.08 MPa,  $\beta$  (decay constant) = 999.25 1/s, and cable element elastic modulus = 2814 MPa [53].

**(a) TM/JCT/SC complex FE model with aqueous outflow**



**(b) TM/JCT complex FE model with embedded collagen fibrils**

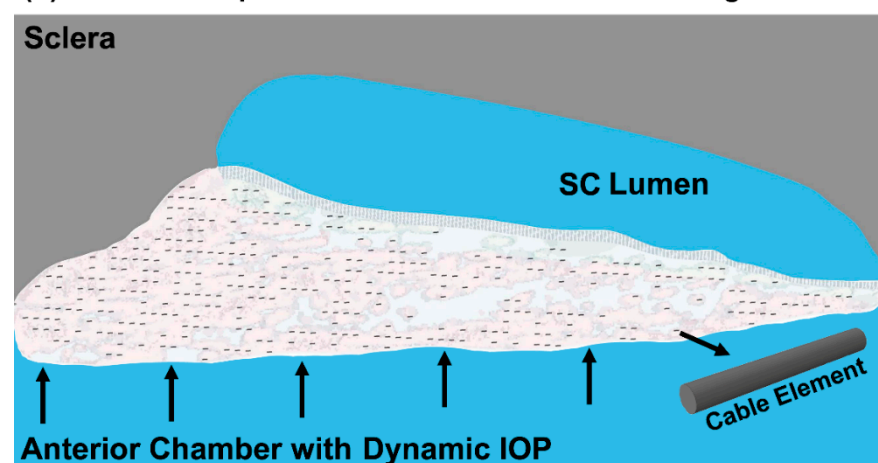


**Figure 1.** (a) The 3D microstructural FE model of the TM/JCT/SC complex and aqueous humor with (b) embedded elastic cable elements [60].

The hydraulic conductivities of  $2.0 \mu\text{L}/\text{min}/\text{mmHg}/\text{cm}^2$  [91],  $2.5 \text{ mmHg}/\mu\text{L}/\text{min}/\text{cm}^2$  [92], and  $9000 \times 10^{-11} \text{ cm}^2 \text{ s}/\text{g}$  [28] were programmed into the model for the TM, JCT, and SC inner wall extracellular matrix [60]. The TM, JCT, and SC inner walls were treated as tissues with the same mechanical properties but different hydraulic conductivities.

A pre-tension force of  $\sim 500 \mu\text{N}$  [93] was induced in the TM/JCT/SC complex local nodes to mimic the ciliary muscle movement during IOP fluctuation [17], which also helps to prevent sudden excessive dynamic response in the cables [52]. Aqueous humor with a physiologic IOP load boundary adopted from a living non-human primate (Figure 2a,b) and an idealized IOP load boundary (Figure 2c) were flowed into the outflow pathway. Due to the limitation in our computational power, only a 400 ms range of physiologic IOP (Figure 2a) was selected and applied to the model (Figure 2b).

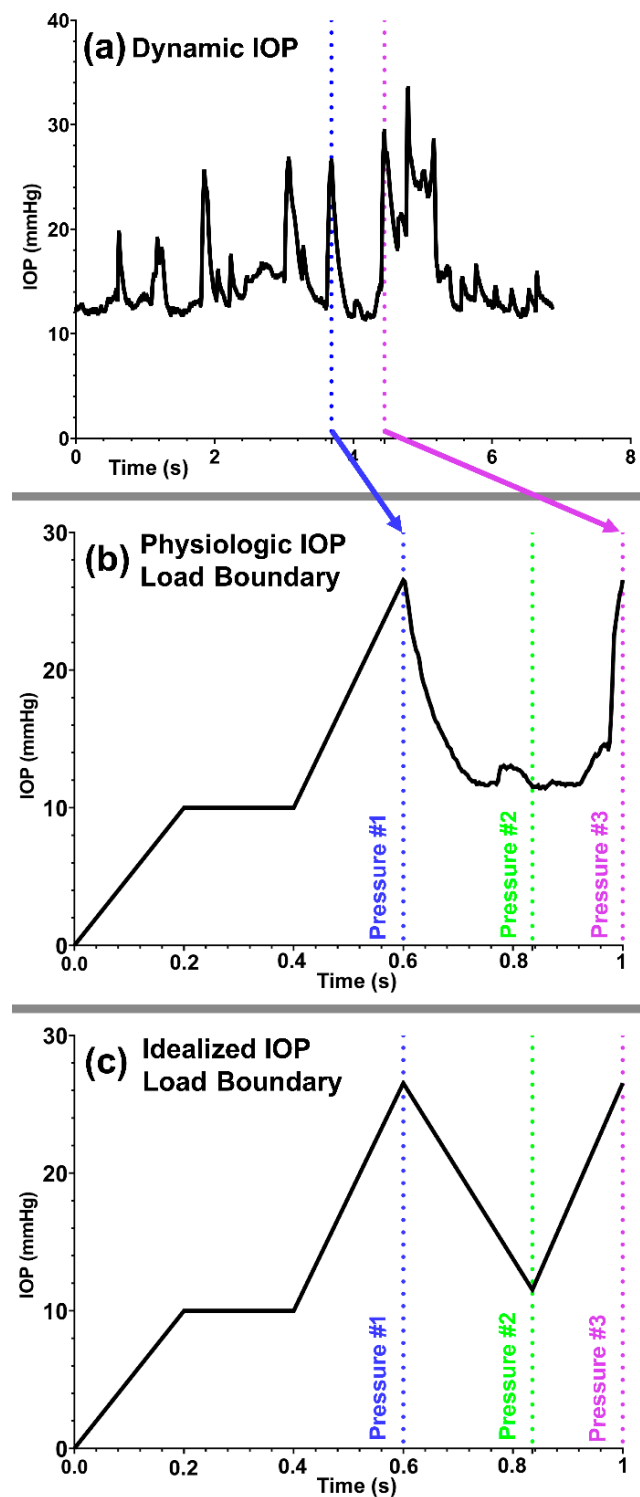


**Figure 2.** (a) Transient IOP fluctuations in a non-human primate (a rhesus macaque aged 4, male, right eye). (b) Physiologic and (c) idealized IOP load boundary with an IOP pre-load applied to the aqueous humor inflow.

### 2.2. Fluid–Structure Interaction

The FSI formulations were fully explained in our prior publication [60]. Briefly, the solid and fluid domains representing the TM/JCT/SC complex and aqueous humor were defined using an arbitrary Lagrangian–Eulerian (ALE) approach [94,95]. The multi material ALE (Ansys/LS-DYNA, Pittsburgh, PA, USA) automatic mesh refinement algorithm helped

to enhance the modeling robustness and accuracy of Lagrangian and Eulerian mesh motions within the same framework, enhancing the modeling ability for curved surfaces of a complex geometry [96,97]. Aqueous humor was modeled as homogeneous, Newtonian, and viscous [98], with the density and dynamic viscosity of  $1000 \text{ kg/m}^3$  and  $0.7185 \text{ mPa}\cdot\text{s}$  [99], respectively.

The pre-load was achieved by a linear IOP elevation to 10 mm Hg for 200 ms (time-step: 10 ms), then kept at 10 mmHg for 200 ms, and finally elevated to 26.54 mmHg for 200 ms. The pre-load was followed by a physiologic IOP load boundary for 400 ms (Figure 2b) [23,100]. An idealized IOP load boundary was also applied within 400 ms after the pre-loading to mimic the same maximum and minimum IOP magnitudes (Figure 2c) that occur in the physiological IOP load boundary (Figure 2b). An explicit dynamic solver was used to solve the problem. The elastic and viscoelastic FSI simulations on average took  $\sim 250$  and  $\sim 436$  h, respectively, to run on our workstation.

### 3. Results

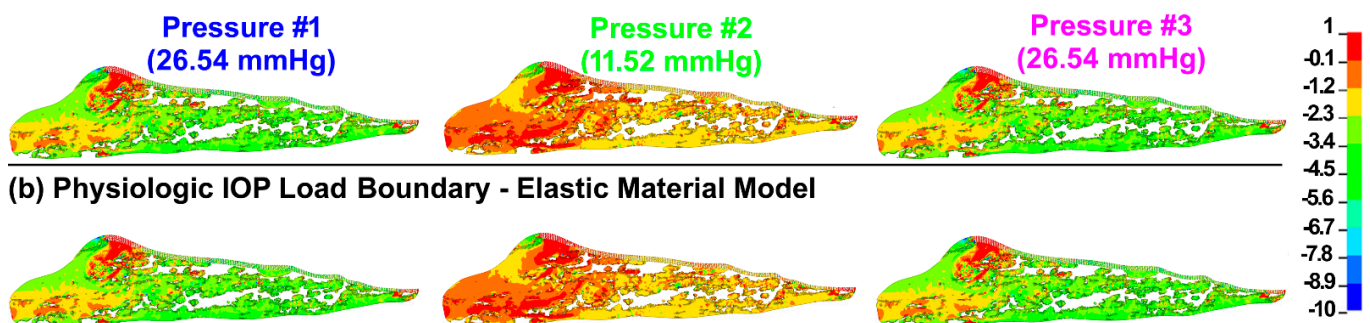
The first principal (tensile) stresses and strains in the TM/JCT/SC complex with idealized and physiologic IOP load boundary and elastic and viscoelastic material models at three different pressures are shown in Figures 3 and 4, respectively.

The maximum shear stresses and strains in the TM/JCT/SC complex with idealized and physiologic IOP load boundary and elastic and viscoelastic material models at three different pressures are shown in Figures 5 and 6, respectively.

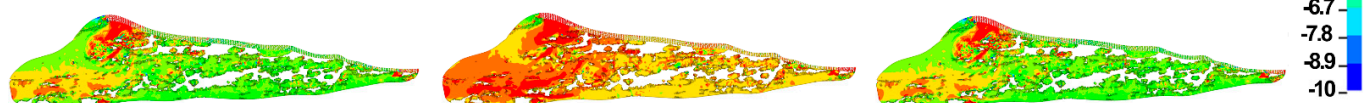
The pressure in the aqueous humor across the TM/JCT/SC complex with idealized and physiologic IOP load boundary and elastic and viscoelastic material models at three different pressures is shown in Figure 7.

## 1st Principal Stress (kPa)

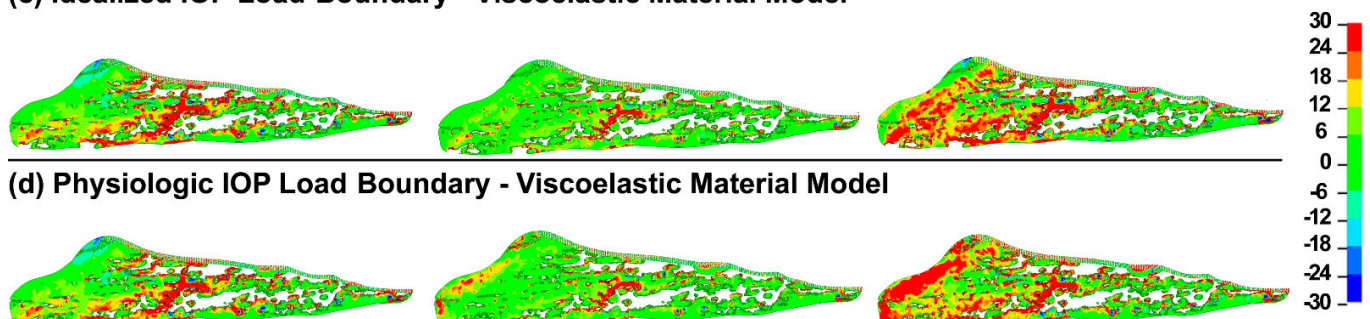
### (a) Idealized IOP Load Boundary - Elastic Material Model



### (b) Physiologic IOP Load Boundary - Elastic Material Model



### (c) Idealized IOP Load Boundary - Viscoelastic Material Model



### (d) Physiologic IOP Load Boundary - Viscoelastic Material Model

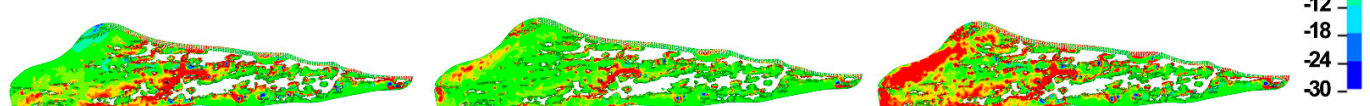
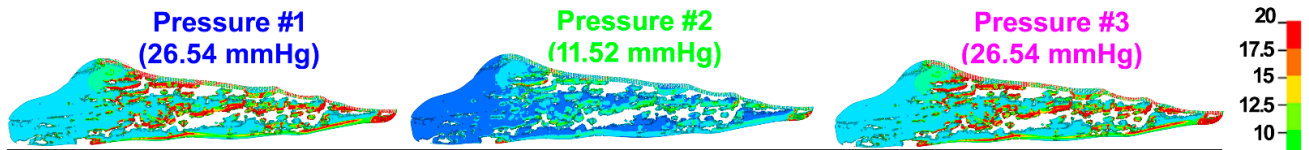


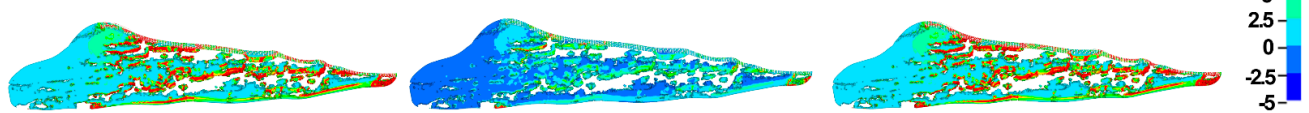
**Figure 3.** The 1st principal stress in the TM/JCT/SC complex with (a) idealized IOP load boundary (elastic material) (pressure t1, pressure t2, pressure t3), (b) physiologic IOP load boundary (elastic material), (c) idealized IOP load boundary (viscoelastic material), and (d) physiologic IOP load boundary (viscoelastic material) at three different IOPs.

### 1st Principal Strain

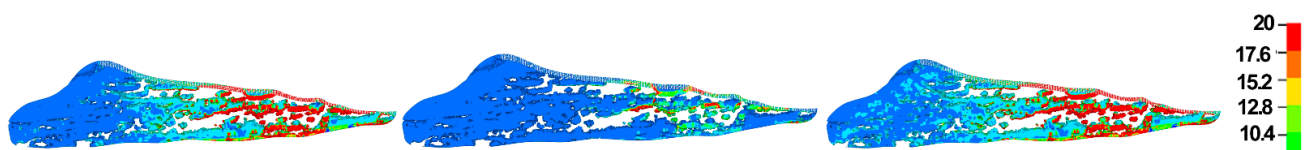
(a) Idealized IOP Load Boundary - Elastic Material Model



(b) Physiologic IOP Load Boundary - Elastic Material Model



(c) Idealized IOP Load Boundary - Viscoelastic Material Model



(d) Physiologic IOP Load Boundary - Viscoelastic Material Model

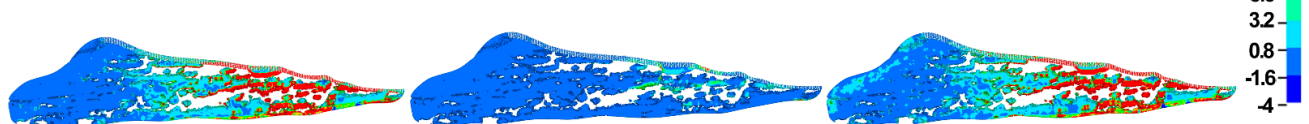


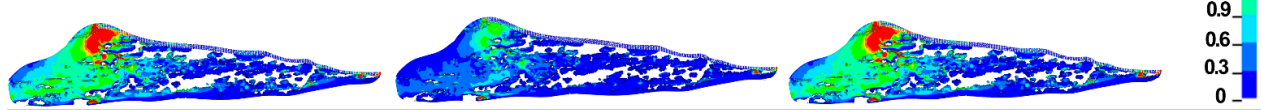
Figure 4. The 1st principal strain in the TM/JCT/SC complex with (a) idealized IOP load boundary (elastic material), (b) physiologic IOP load boundary (elastic material), (c) idealized IOP load boundary (viscoelastic material), and (d) physiologic IOP load boundary (viscoelastic material) at three different IOPs.

### Maximum Shear Stress (kPa)

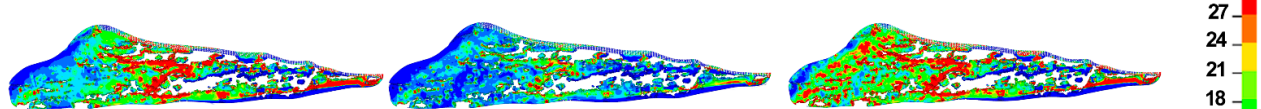
(a) Idealized IOP Load Boundary - Elastic Material Model



(b) Physiologic IOP Load Boundary - Elastic Material Model



(c) Idealized IOP Load Boundary - Viscoelastic Material Model



(d) Physiologic IOP Load Boundary - Viscoelastic Material Model

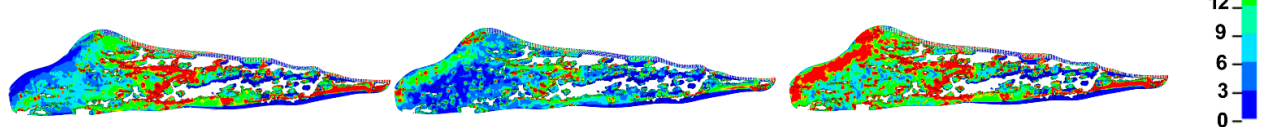


Figure 5. The maximum shear stress in the TM/JCT/SC complex with (a) idealized IOP load boundary (elastic material), (b) physiologic IOP load boundary (elastic material), (c) idealized IOP load boundary (viscoelastic material), and (d) physiologic IOP load boundary (viscoelastic material) at three different IOPs.

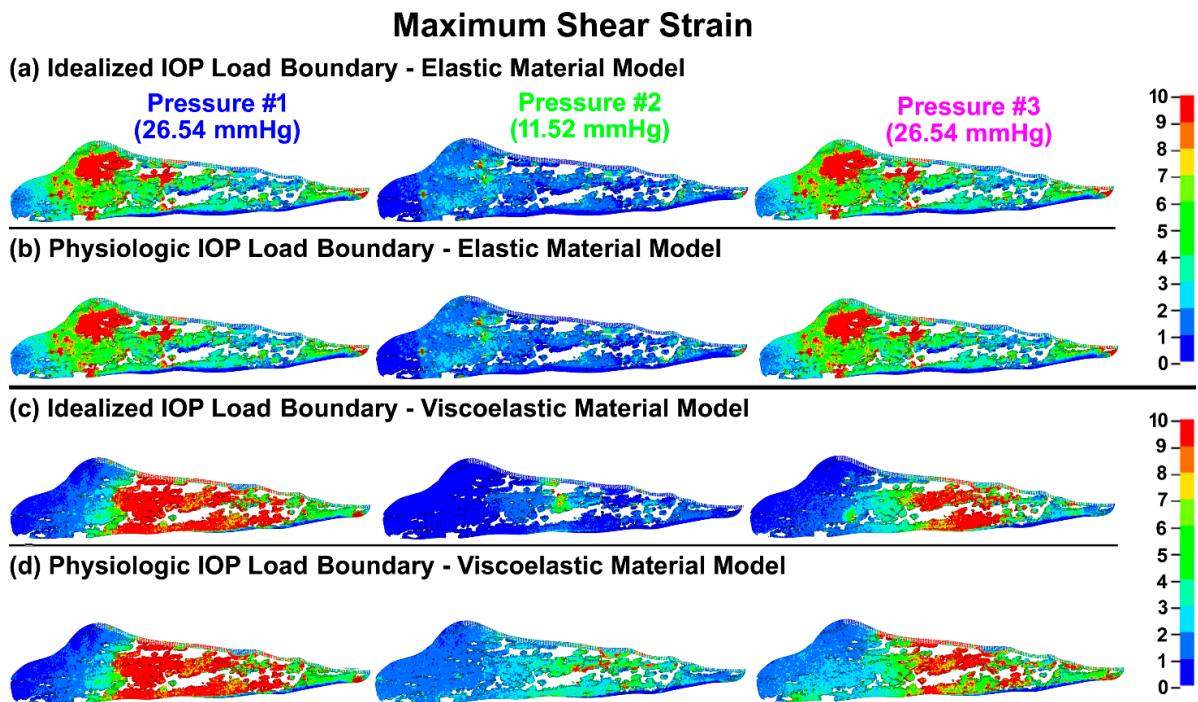


Figure 6. The maximum shear strain in the TM/JCT/SC complex with (a) idealized IOP load boundary (elastic material), (b) physiologic IOP load boundary (elastic material), (c) idealized IOP load boundary (viscoelastic material), and (d) physiologic IOP load boundary (viscoelastic material) at three different IOPs.

### Aqueous Humor Pressure (mmHg)

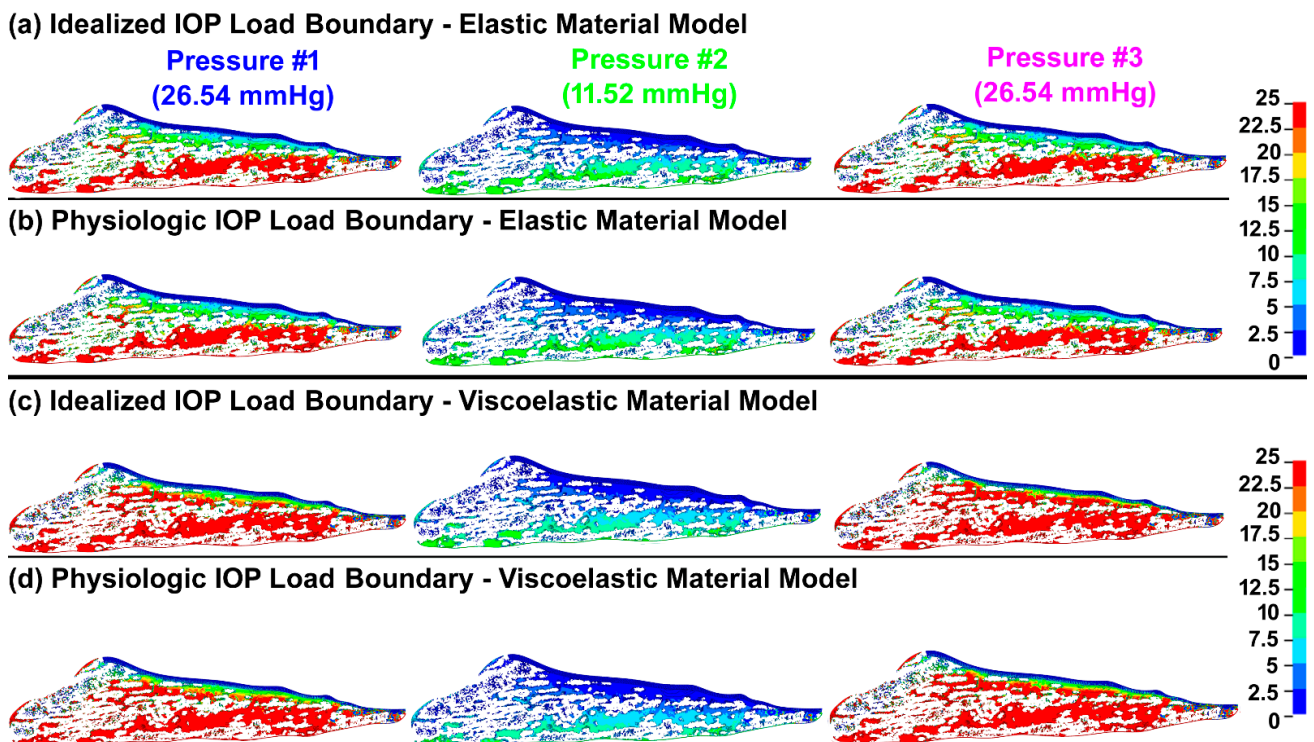
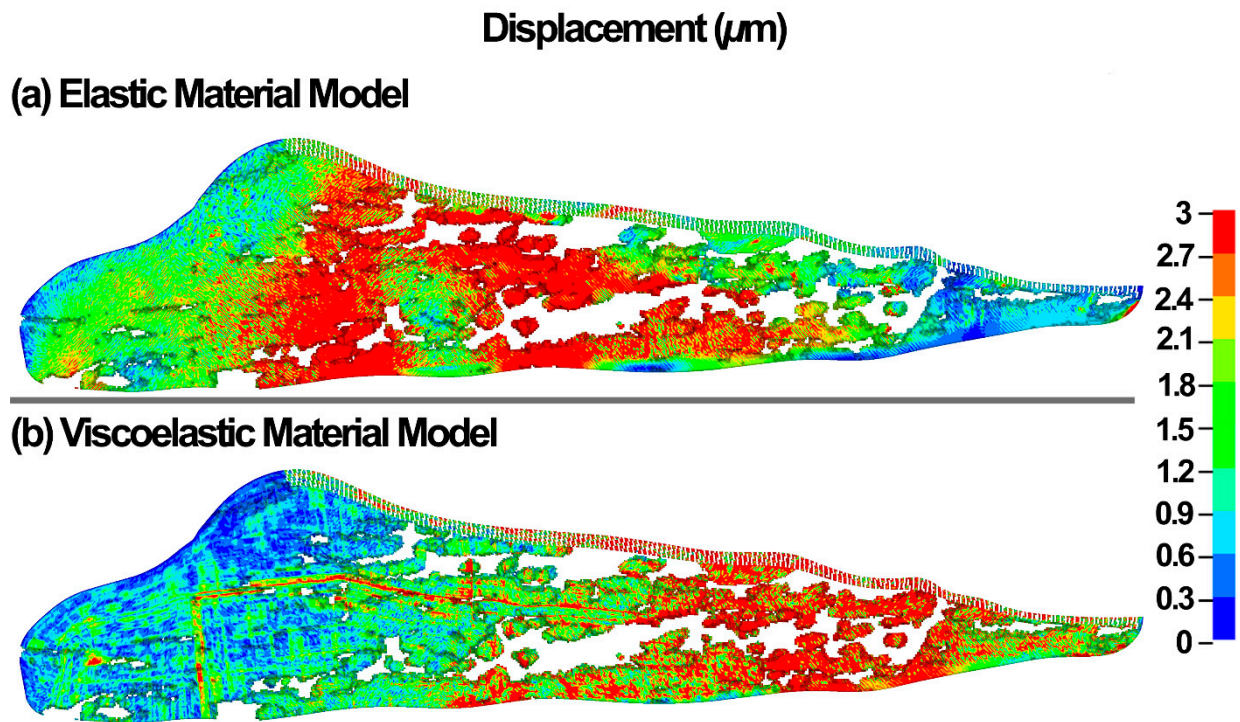


Figure 7. The pressure in the aqueous humor across the TM/JCT/SC complex with (a) idealized IOP load boundary (elastic material), (b) physiologic IOP load boundary (elastic material), (c) idealized IOP load boundary (viscoelastic material), and (d) physiologic IOP load boundary (viscoelastic material) at three different IOPs.

The resultant displacement in the TM/JCT/SC complex at the IOP of 10 mmHg is shown in Figure 8.



**Figure 8.** The displacement in the TM/JCT/SC complex with (a) elastic and (b) viscoelastic material model at the IOP of 10 mmHg.

The volumetric average stresses and strains in the TM/JCT/SC complex, as well as the average volumetric pressure in the aqueous humor across the TM/JCT/SC complex, are summarized in Table 1.

**Table 1.** Volumetric average stresses and strains in the TM/JCT/SC complex and volumetric average pressure in the aqueous humor.

Simulations	1st Principal Stress (kPa)	1st Principal Strain (%)	Max Shear Stress (kPa)	Max Shear Strain (%)	AH Pressure (mmHg)
<b>Idealized IOP Load Boundary—Elastic Material Model</b>					
Pressure #1	−3.18	4.83	0.68	4.55	13.88
Pressure #2	−1.17	1.22	0.35	1.95	4.02
Pressure #3	−3.17	4.83	0.69	4.55	13.88
<b>Physiologic IOP Load Boundary—Elastic Material Model</b>					
Pressure #1	−3.18	4.83	0.68	4.55	13.88
Pressure #2	−1.17	1.22	0.35	1.95	4.02
Pressure #3	−3.17	4.83	0.69	4.54	13.88
<b>Idealized IOP Load Boundary—Viscoelastic Material Model</b>					
Pressure #1	−4.95	2.15	9.84	7.66	12.01
Pressure #2	−3.12	0.92	4.12	2.29	3.98
Pressure #3	−6.12	2.22	10.65	4.55	11.11
<b>Physiologic IOP Load Boundary—Viscoelastic Material Model</b>					
Pressure #1	−4.95	2.15	9.84	7.66	12.01
Pressure #2	−2.99	0.79	4.75	2.93	4.35
Pressure #3	−5.41	2.33	11.59	3.89	11.42

#### 4. Discussion

Characterizing the mechanical behavior of the outflow tissues with a dynamic IOP load boundary may significantly contribute to our understanding of IOP regulation in the human eye [17]. Aqueous outflow resistance in the conventional outflow pathway is the predominant parameter in providing a balance between the average rate of aqueous inflow and outflow to maintain IOP within the normal physiologic range [59]. Experimental [59,74,101–105] and numerical [106–108] studies to date, and reviews of their findings [9,10,17,109–115], have all contributed greatly to our understanding of the mechanism of outflow resistance in the conventional outflow pathway. However, the active biomechanical response of the outflow tissues and their interaction with aqueous humor outflow dynamics have not been determined. The outflow pathway pressure provides a very dynamic mechanical environment that actively affects the tissues' geometry [59,116] and causes a time-dependent pressure gradient across the outflow tissues [9,29]. Outflow resistance is affected by alterations in tissue geometry [117], so there must be a coupling between outflow hydrodynamics (fluid) and the biomechanics of the TM, JCT, and SC inner wall (structure) in the form of a fluid–structure interaction [58]. This coupling has been proven through experimental studies showing a correlation between the biomechanics of the outflow tissues and the rate of the aqueous outflow [57,59], suggesting that the outflow resistance actively contributes to aqueous outflow regulation to maintain an IOP within the normal range. In this study, a 3D FE microstructural model of the human TM/JCT/SC complex was constructed [60] (Figure 1) and subjected to an aqueous inflow with an idealized (steady flow) and physiologic IOP (pulsatile flow) load boundary (Figure 2). Outflow tissues were treated as elastic and viscoelastic. The material parameters were obtained from our prior study using an FE-optimization algorithm for healthy eyes matched with PhS-OCT imaging data [53].

Elastic materials behave the same regardless of time and loading rate, so the final resultant strain will be the same when load rate or time change [118]. As such, the first principal (tensile) stresses and strains in the TM/JCT/SC complex model with the elastic material model were similar regardless of the rate of the applied IOP load (Figures 3 and 4; Table 1). The viscoelastic FE model showed larger stresses but smaller strains across the TM/JCT/SC complex than the elastic model (Figures 3 and 4; Table 1). Transient IOP fluctuations cause a relatively large IOP difference (~20 mmHg) in a very short time frame (~0.1 s) (Figure 2a) that may result in viscoelastic rate stiffening in the outflow tissues. Rate stiffening reduces strains and causes a rate-dependent outflow pressure gradient across the outflow tissues, as observed in our modeling results (Figure 4 and Table 1). In the elastic TM/JCT/SC complex FE model, the strain appears immediately once the IOP load boundary is applied to the tissues. The strain is larger (Figures 3 and 4; Table 1) and proportional to the applied IOP load boundary, which is different than the results from the viscoelastic model (Table 1). The viscous component of the viscoelastic material deforms slowly when exposed to an external force. Once a deforming force has been removed, the elastic portion of the material returns the tissue to its original configuration [119]. Viscoelastic materials present a reversible response depending on the rate of the applied load as they can return to the initial state [120–122], and this is why the resultant stresses and strains across the outflow connective tissues are IOP load rate-dependent (Figures 3 and 4; Table 1).

TM biomechanics appears to be a key regulator of mechanosensing within the conventional outflow pathway [108]. When the TM expands with IOP elevation, it stretches the TM lamellae [2,29,57,123,124] and induces shear stress (Figure 5) and strain (Figure 6) in the SC endothelial cells due to circumferential flow through a narrowing SC lumen [125,126]. Calculating the shear stress of a viscoelastic outflow tissue with a physiologic IOP load boundary may significantly contribute to our understanding of IOP regulation through the endothelial nitric oxide pathway [67–69]. Viscoelastic outflow tissues showed a larger shear strain than elastic tissues (Figure 6 and Table 1). Shear strain in the viscoelastic FE model at pressure #1 was larger than in pressure #3 (Figure 6 and Table 1). While the magnitude of the pressure at these two points was the same at 26.5 mmHg, the IOP history was different

(Figure 2b), which affects the tissue's shear strain. In response to a shear strain, SC cells actively upregulate nitric oxide production, relaxing neighboring TM cells and increasing the permeability of the SC inner wall [67–69].

The TM/JCT interface and the inner wall of SC as well as distal to the outer wall of SC are predominantly responsible for ~50–75% and ~25–50% of the outflow resistance, respectively [58,62,127–130]. While the outflow resistance in the elastic FE model mainly resides within the TM/JCT, in the viscoelastic model, the JCT and the immediate vicinity of the SC inner wall are the main site of the outflow resistance (Figure 7). Aqueous outflow resistance results in a pressure gradient [9,30] in the outflow tissues that impacts the outflow system homeostasis and contributes to maintaining IOP in the normal range [131,132]. The pressure gradient also changes the outflow tissues' geometry [25–27], which in turn affects the loading regime across the tissues, as well as the outflow resistance [28].

Li and colleagues showed that at a constant ocular pulse amplitude, the resultant TM displacement is IOP magnitude-dependent, whereby a larger IOP causes smaller displacement in the TM [33]. The smaller displacement suggests that the TM tissue must be viscoelastic. Li showed the average TM displacement of ~1.6  $\mu\text{m}$  at an IOP of 10 mmHg [33]. In our study, the elastic and viscoelastic models resulted in the nodal-averaged TM displacements of ~2.0 and 1.5  $\mu\text{m}$  at an IOP of 10 mmHg (Figure 8). Li [33] used nonhuman primate eyes (*Macaca nemestrina*) and we modeled human eyes, so the difference in TM displacements we report could be due to species-related differences in biomechanical tissue properties.

#### Limitations

First, the geometries of the JCT and SC inner wall were considered as part of the segmented, reconstructed TM FE microstructure. However, we did not have any eye-specific dimensions for the JCT and SC inner wall, so they were reconstructed based on their average thicknesses from the literature: ~10  $\mu\text{m}$  [71] and ~5  $\mu\text{m}$  [30] for the JCT and SC inner wall, respectively. In addition, the  $\mu\text{m}$ -sized pores in the SC inner wall were not eye-specific and were distributed based on the data available in the literature with the density and size of 835 pores/ $\text{mm}^2$  [30] and 1.3  $\mu\text{m}$  [75], respectively. While this study assumes pores are not artifactual, some may have different opinions and say pores are artifacts due to fixation. It has been shown that pore density in the SC inner wall decreases with reduced fixation time [30,75,112,133]. However, the in vivo existence of SC inner wall pores may need further clarification [112], which is outside of the scope of this study. Outflow is segmental with high- and low-flow regions, and one proposed route for the aqueous humor drainage across the inner wall is through giant vacuoles. Studies hypothesize that aqueous then passes through intercellular and intracellular pores [134]. An alternative to pores as a mechanism of aqueous passage from the JCT region to SC has been documented in multiple studies [17,135,136]. Funnel-like conduits arise from the SC inner wall endothelium and cross the SC to attach to the external wall. These aqueous flow conduits connect the TM and distal pathways, leading to TM and distal pathway synchronous motion [17]. Evidence suggests that modeling flow pathways distal to the TM would be valuable, but that is outside the scope of the current study.

Second, the same mechanical properties were used for the TM, JCT, and SC inner wall, but they have different properties. Although the differences could be a limitation of this study, the viscoelastic mechanical properties of the TM, JCT, and SC inner wall as separate tissues are still unknown. In a future study, we will calculate the mechanical properties of the TM, JCT, and SC inner wall separately using the FE-optimization algorithm matching with PhS-OCT imaging data.

Third, only one IOP cycle was simulated herein; the resultant stresses and strains may show larger differences if the simulation is performed in several loading cycles. In future studies, we will attempt to perform simulations with several IOP cycles.

Finally, this pilot study explored the feasibility of characterizing the viscoelasticity and dynamic IOP relationships and their resultant stresses and strains. Future studies

will benefit from a larger cohort of healthy eyes to better generalize the tissues' accurate geometry and biomechanical responses.

## 5. Conclusions

A 3D eye-specific elastic and viscoelastic microstructural FE model of a healthy human outflow pathway was established and subjected to both idealized and physiologic IOP load boundaries. This model allowed us to calculate the stresses and strains in the outflow tissues and the hydrodynamics of the aqueous humor. The results revealed that while the viscoelastic material model includes the IOP load rate in the resultant stresses and strains across the outflow pathway, the elastic material model results in the same stresses and strains regardless of the IOP load rate. The outflow pathway is subjected to a very dynamic, physiologic IOP load boundary and these model results suggest that the parameters should include and consider the applied IOP load rate to better estimate the stresses and strains in the outflow tissues and the hydrodynamics of the aqueous humor. The improved understanding may contribute to our knowledge of aqueous outflow dynamic regulation in the conventional outflow pathway.

**Author Contributions:** Conceptualization, A.K.; methodology, A.K., R.R., S.M.R., R.K.W. and M.J.K.; software, A.K., R.R. and S.M.R.; validation, A.K., R.R., S.M.R., R.K.W. and M.J.; formal analysis, A.K., R.R., S.M.R., R.K.W. and M.J.; investigation, A.K., R.R., S.M.R., R.K.W. and M.J.; resources, A.K., T.S.A., M.J.K., R.K.W., M.J. and J.C.D.; data curation, A.K., T.S.A., M.J.K., R.K.W., M.J. and J.C.D.; writing—original draft preparation, A.K.; writing—review and editing, A.K., T.S.A., M.J.K., R.K.W., M.J. and J.C.D.; visualization, A.K.; supervision, A.K., T.S.A., M.J.K., R.K.W., M.J. and J.C.D.; project administration, A.K.; funding acquisition, J.C.D. All authors have read and agreed to the published version of the manuscript.

**Funding:** This work was supported in part by the National Institutes of Health Grants R01-EY027924, R01-EY018926, and P30-EY003039 (Bethesda, Maryland); EyeSight Foundation of Alabama (Birmingham, Alabama); and Research to Prevent Blindness (New York, NY).

**Institutional Review Board Statement:** The Internal Review Board of the Portland at Oregon Health & Science University approved the experimental section. This study also entirely adhered to the 2008 declaration of Helsinki.

**Informed Consent Statement:** Written informed consent was obtained from the family of all subjects involved in the study. The subject gave his informed consent for inclusion before he participated in this study. The study was conducted in accordance with the Declaration of Helsinki, and the protocol was approved by the ethics committee of the Portland at Oregon Health & Science University.

**Data Availability Statement:** The raw/processed data required to reproduce these findings cannot be shared at this time as the data is part of an ongoing study.

**Conflicts of Interest:** The authors declare that they have no known competing financial interest or personal relationships that could have appeared to influence the work reported in this paper.

## References

1. Ellingsen, B.A.; Grant, W.M. The relationship of pressure and aqueous outflow in enucleated human eyes. *Investig. Ophthalmol.* **1971**, *10*, 430–437.
2. Moses, R.A. The effect of intraocular pressure on resistance to outflow. *Surv. Ophthalmol.* **1977**, *22*, 88–100. [[CrossRef](#)]
3. Johnson, M.C.; Kamm, R.D. The role of Schlemm's canal in aqueous outflow from the human eye. *Investig. Ophthalmol. Vis. Sci.* **1983**, *24*, 320–325.
4. Johnson, D.H.; Johnson, M. How does nonpenetrating glaucoma surgery work? Aqueous outflow resistance and glaucoma surgery. *J. Glaucoma* **2001**, *10*, 55–67. [[CrossRef](#)]
5. Kitazawa, Y.; Horie, T. Diurnal variation of intraocular pressure in primary open-angle glaucoma. *Am. J. Ophthalmol.* **1975**, *79*, 557–566. [[CrossRef](#)]
6. Sommer, A.; Tielsch, J.M.; Katz, J.; Quigley, H.A.; Gottsch, J.D.; Javitt, J.; Singh, K. Relationship between intraocular pressure and primary open angle glaucoma among white and black Americans. The Baltimore Eye Survey. *Arch. Ophthalmol.* **1991**, *109*, 1090–1095. [[CrossRef](#)]
7. Fautsch, M.P.; Johnson, D.H.; Group, S.A.P.R.I.W. Aqueous humor outflow: What do we know? Where will it lead us? *Investig. Ophthalmol. Vis. Sci.* **2006**, *47*, 4181–4187. [[CrossRef](#)]

8. Kwon, Y.H.; Fingert, J.H.; Kuehn, M.H.; Alward, W.L. Primary open-angle glaucoma. *N. Engl. J. Med.* **2009**, *360*, 1113–1124. [[CrossRef](#)]
9. Goel, M.; Picciani, R.G.; Lee, R.K.; Bhattacharya, S.K. Aqueous humor dynamics: A review. *Open Ophthalmol. J.* **2010**, *4*, 52–59. [[CrossRef](#)]
10. Stamer, W.D.; Acott, T.S. Current understanding of conventional outflow dysfunction in glaucoma. *Curr. Opin. Ophthalmol.* **2012**, *23*, 135–143. [[CrossRef](#)]
11. Tamm, E. Glaucoma opinion: A unifying concept for trabecular meshwork pathology in primary open angle glaucoma. *Int. Glaucoma Rev.* **2013**, *15*, 45–47.
12. Carreon, T.; van der Merwe, E.; Fellman, R.L.; Johnstone, M.; Bhattacharya, S.K. Aqueous outflow—A continuum from trabecular meshwork to episcleral veins. *Prog. Retin. Eye Res.* **2017**, *57*, 108–133. [[CrossRef](#)] [[PubMed](#)]
13. Dvorak-Theobald, G.; Kirk, H.Q. Aqueous pathways in some cases of glaucoma. *Trans. Am. Ophthalmol. Soc.* **1955**, *53*, 301.
14. Johnstone, M.A. The aqueous outflow system as a mechanical pump: Evidence from examination of tissue and aqueous movement in human and non-human primates. *J. Glaucoma* **2004**, *13*, 421–438. [[CrossRef](#)]
15. Johnstone, M.; Jamil, A.; Martin, E. Aqueous veins and open angle glaucoma. In *The Glaucoma Book*; Springer: Berlin/Heidelberg, Germany, 2010; pp. 65–78.
16. Johnstone, M.A. Intraocular pressure regulation: Findings of pulse-dependent trabecular meshwork motion lead to unifying concepts of intraocular pressure homeostasis. *J. Ocul. Pharmacol. Ther.* **2014**, *30*, 88–93. [[CrossRef](#)]
17. Johnstone, M.; Xin, C.; Tan, J.; Martin, E.; Wen, J.; Wang, R.K. Aqueous outflow regulation—21st century concepts. *Prog. Retin. Eye Res.* **2020**, *83*, 100917. [[CrossRef](#)] [[PubMed](#)]
18. Ascher, K.W. *The Aqueous Veins: Biomicroscopic Study of the Aqueous Humor Elimination*; Thomas: Minneapolis, MN, USA, 1961.
19. Johnstone, M.; Martin, E.; Jamil, A. Pulsatile flow into the aqueous veins: Manifestations in normal and glaucomatous eyes. *Exp. Eye Res.* **2011**, *92*, 318–327. [[CrossRef](#)] [[PubMed](#)]
20. Downs, J.C. IOP telemetry in the nonhuman primate. *Exp. Eye Res.* **2015**, *141*, 91–98. [[CrossRef](#)]
21. Xin, C.; Wang, R.K.; Song, S.; Shen, T.; Wen, J.; Martin, E.; Jiang, Y.; Padilla, S.; Johnstone, M. Aqueous outflow regulation: Optical coherence tomography implicates pressure-dependent tissue motion. *Exp. Eye Res.* **2017**, *158*, 171–186. [[CrossRef](#)]
22. Turner, D.C.; Samuels, B.C.; Huisinigh, C.; Girkin, C.A.; Downs, J.C. The Magnitude and Time Course of IOP Change in Response to Body Position Change in Nonhuman Primates Measured Using Continuous IOP Telemetry. *Investig. Ophthalmol. Vis. Sci.* **2017**, *58*, 6232–6240. [[CrossRef](#)]
23. Turner, D.C.; Edmiston, A.M.; Zohner, Y.E.; Byrne, K.J.; Seigfreid, W.P.; Girkin, C.A.; Morris, J.S.; Downs, J.C. Transient Intraocular Pressure Fluctuations: Source, Magnitude, Frequency, and Associated Mechanical Energy. *Investig. Ophthalmol. Vis. Sci.* **2019**, *60*, 2572–2582. [[CrossRef](#)] [[PubMed](#)]
24. Turner, D.C.; Girkin, C.A.; Downs, J.C. The Magnitude of IOP Elevation Associated with Eye Rubbing. *Ophthalmology* **2019**, *126*, 171. [[CrossRef](#)] [[PubMed](#)]
25. Lei, Y.; Stamer, W.D.; Wu, J.; Sun, X. Cell senescence reduced the mechanotransduction sensitivity of porcine angular aqueous plexus cells to elevation of pressure. *Investig. Ophthalmol. Vis. Sci.* **2014**, *55*, 2324–2328. [[CrossRef](#)]
26. Overby, D.R.; Zhou, E.H.; Vargas-Pinto, R.; Pedrigi, R.M.; Fuchshofer, R.; Braakman, S.T.; Gupta, R.; Perkumas, K.M.; Sherwood, J.M.; Vahabikashi, A.; et al. Altered mechanobiology of Schlemm’s canal endothelial cells in glaucoma. *Proc. Natl. Acad. Sci. USA* **2014**, *111*, 13876–13881. [[CrossRef](#)]
27. Stamer, W.D.; Braakman, S.T.; Zhou, E.H.; Ethier, C.R.; Fredberg, J.J.; Overby, D.R.; Johnson, M. Biomechanics of Schlemm’s canal endothelium and intraocular pressure reduction. *Prog. Retin. Eye Res.* **2015**, *44*, 86–98. [[CrossRef](#)] [[PubMed](#)]
28. Johnson, M. What controls aqueous humour outflow resistance? *Exp. Eye Res.* **2006**, *82*, 545–557. [[CrossRef](#)]
29. Johnstone, M.A.; Grant, W.G. Pressure-dependent changes in structures of the aqueous outflow system of human and monkey eyes. *Am. J. Ophthalmol.* **1973**, *75*, 365–383. [[CrossRef](#)]
30. Johnson, M.; Chan, D.; Read, A.T.; Christensen, C.; Sit, A.; Ethier, C.R. The pore density in the inner wall endothelium of Schlemm’s canal of glaucomatous eyes. *Investig. Ophthalmol. Vis. Sci.* **2002**, *43*, 2950–2955.
31. Gao, K.; Song, S.; Johnstone, M.A.; Zhang, Q.; Xu, J.; Zhang, X.; Wang, R.K.; Wen, J.C. Reduced Pulsatile Trabecular Meshwork Motion in Eyes With Primary Open Angle Glaucoma Using Phase-Sensitive Optical Coherence Tomography. *Investig. Ophthalmol. Vis. Sci.* **2020**, *61*, 21. [[CrossRef](#)]
32. Xin, C.; Wang, X.F.; Wang, N.L.; Wang, R.K.; Johnstone, M. Trabecular Meshwork Motion Profile from Pulsatile Pressure Transients: A New Platform to Simulate Transitory Responses in Humans and Nonhuman Primates. *Appl. Sci.* **2022**, *12*, 11. [[CrossRef](#)]
33. Li, P.; Reif, R.; Zhi, Z.; Martin, E.; Shen, T.T.; Johnstone, M.; Wang, R.K. Phase-sensitive optical coherence tomography characterization of pulse-induced trabecular meshwork displacement in ex vivo nonhuman primate eyes. *J. Biomed. Opt.* **2012**, *17*, 076026. [[CrossRef](#)] [[PubMed](#)]
34. Li, P.; Shen, T.T.; Johnstone, M.; Wang, R.K. Pulsatile motion of the trabecular meshwork in healthy human subjects quantified by phase-sensitive optical coherence tomography. *Biomed. Opt. Express* **2013**, *4*, 2051–2065. [[CrossRef](#)] [[PubMed](#)]
35. Xin, C.; Song, S.; Johnstone, M.; Wang, N.; Wang, R.K. Quantification of Pulse-Dependent Trabecular Meshwork Motion in Normal Humans Using Phase-Sensitive OCT. *Investig. Ophthalmol. Vis. Sci.* **2018**, *59*, 3675–3681. [[CrossRef](#)] [[PubMed](#)]
36. Gao, K.; Song, S.Z.; Johnstone, M.A.; Wang, R.K.K.; Wen, J.C. Trabecular Meshwork Motion in Normal Compared with Glaucoma Eyes. *Investig. Ophthalmol. Vis. Sci.* **2019**, *60*, 4824.

37. Du, R.; Xin, C.; Xu, J.; Hu, J.; Wang, H.; Wang, N.; Johnstone, M. Pulsatile Trabecular Meshwork Motion: An Indicator of Intraocular Pressure Control in Primary Open-Angle Glaucoma. *J. Clin. Med.* **2022**, *11*, 2696. [[CrossRef](#)]
38. Wang, K.; Read, A.T.; Sulchek, T.; Ethier, C.R. Trabecular meshwork stiffness in glaucoma. *Exp. Eye Res.* **2017**, *158*, 3–12. [[CrossRef](#)]
39. Last, J.A.; Pan, T.; Ding, Y.; Reilly, C.M.; Keller, K.; Acott, T.S.; Fautsch, M.P.; Murphy, C.J.; Russell, P. Elastic modulus determination of normal and glaucomatous human trabecular meshwork. *Investig. Ophthalmol. Vis. Sci.* **2011**, *52*, 2147–2152. [[CrossRef](#)]
40. Li, G.; Lee, C.; Agrahari, V.; Wang, K.; Navarro, I.; Sherwood, J.M.; Crews, K.; Farsiu, S.; Gonzalez, P.; Lin, C.W.; et al. In vivo measurement of trabecular meshwork stiffness in a corticosteroid-induced ocular hypertensive mouse model. *Proc. Natl. Acad. Sci. USA* **2019**, *116*, 1714–1722. [[CrossRef](#)]
41. Wang, K.; Johnstone, M.A.; Xin, C.; Song, S.; Padilla, S.; Vranka, J.A.; Acott, T.S.; Zhou, K.; Schwaner, S.A.; Wang, R.K.; et al. Estimating Human Trabecular Meshwork Stiffness by Numerical Modeling and Advanced OCT Imaging. *Investig. Ophthalmol. Vis. Sci.* **2017**, *58*, 4809–4817. [[CrossRef](#)]
42. Dehoff, P.H. On the nonlinear viscoelastic behavior of soft biological tissues. *J. Biomech.* **1978**, *11*, 35–40. [[CrossRef](#)]
43. Humphrey, J.D. Continuum biomechanics of soft biological tissues. *Proc. R. Soc. A-Math. Phys. Eng. Sci.* **2003**, *459*, 3–46. [[CrossRef](#)]
44. Karimi, A.; Shojaei, A.; Razaghi, R. Viscoelastic mechanical measurement of the healthy and atherosclerotic human coronary arteries using DIC technique. *Artery Res.* **2017**, *18*, 14–21. [[CrossRef](#)]
45. Holzapfel, G.A. Similarities between soft biological tissues and rubberlike materials. In *Constitutive Models for Rubber IV*; Routledge: London, UK, 2017; pp. 607–617.
46. Maccabi, A.; Shin, A.; Namiri, N.K.; Bajwa, N.; St John, M.; Taylor, Z.D.; Grundfest, W.; Saddik, G.N. Quantitative characterization of viscoelastic behavior in tissue-mimicking phantoms and ex vivo animal tissues. *PLoS ONE* **2018**, *13*, e0191919. [[CrossRef](#)]
47. Estermann, S.J.; Pahr, D.H.; Reisinger, A. Material design of soft biological tissue replicas using viscoelastic micromechanical modelling. *J. Mech. Behav. Biomed. Mater.* **2022**, *125*, 104875. [[CrossRef](#)]
48. Fung, Y.-C. Bio-viscoelastic solids. In *Biomechanics*; Springer: Berlin/Heidelberg, Germany, 1981; pp. 196–260.
49. Filla, M.S.; Schwinn, M.K.; Nosie, A.K.; Clark, R.W.; Peters, D.M. Dexamethasone-associated cross-linked actin network formation in human trabecular meshwork cells involves beta3 integrin signaling. *Investig. Ophthalmol. Vis. Sci.* **2011**, *52*, 2952–2959. [[CrossRef](#)]
50. Clark, R.; Nosie, A.; Walker, T.; Faralli, J.A.; Filla, M.S.; Barrett-Wilt, G.; Peters, D.M. Comparative genomic and proteomic analysis of cytoskeletal changes in dexamethasone-treated trabecular meshwork cells. *Mol. Cell Proteom.* **2013**, *12*, 194–206. [[CrossRef](#)]
51. Vranka, J.A.; Kelley, M.J.; Acott, T.S.; Keller, K.E. Extracellular matrix in the trabecular meshwork: Intraocular pressure regulation and dysregulation in glaucoma. *Exp. Eye Res.* **2015**, *133*, 112–125. [[CrossRef](#)]
52. Karimi, A.; Rahmati, S.M.; Razaghi, R.; Girkin, C.A.; Crawford Downs, J. Finite element modeling of the complex anisotropic mechanical behavior of the human sclera and pia mater. *Comput. Methods Programs Biomed.* **2022**, *215*, 106618. [[CrossRef](#)]
53. Karimi, A.; Rahmati, S.M.; Razaghi, R.; Crawford Downs, J.; Acott, T.S.; Wang, R.K.; Johnstone, M. Biomechanics of human trabecular meshwork in healthy and glaucoma eyes via dynamic Schlemm’s canal pressurization. *Comput. Methods Programs Biomed.* **2022**, *221*, 106921. [[CrossRef](#)]
54. Fung, Y.C. Biorheology of soft tissues. *Biorheology* **1973**, *10*, 139–155. [[CrossRef](#)]
55. Fung, Y.-C. The meaning of the constitutive equation. In *Biomechanics*; Springer: Berlin/Heidelberg, Germany, 1993; pp. 23–65.
56. Snoeijer, J.H.; Pandey, A.; Herrada, M.A.; Eggens, J. The relationship between viscoelasticity and elasticity. *Proc. Math Phys. Eng. Sci.* **2020**, *476*, 20200419. [[CrossRef](#)] [[PubMed](#)]
57. Bradley, J.M.; Kelley, M.J.; Zhu, X.; Anderssohn, A.M.; Alexander, J.P.; Acott, T.S. Effects of mechanical stretching on trabecular matrix metalloproteinases. *Investig. Ophthalmol. Vis. Sci.* **2001**, *42*, 1505–1513.
58. Overby, D.R.; Stamer, W.D.; Johnson, M. The changing paradigm of outflow resistance generation: Towards synergistic models of the JCT and inner wall endothelium. *Exp. Eye Res.* **2009**, *88*, 656–670. [[CrossRef](#)]
59. Ramos, R.F.; Stamer, W.D. Effects of cyclic intraocular pressure on conventional outflow facility. *Investig. Ophthalmol. Vis. Sci.* **2008**, *49*, 275–281. [[CrossRef](#)] [[PubMed](#)]
60. Karimi, A.; Razaghi, R.; Rahmati, S.M.; Downs, J.C.; Acott, T.S.; Wang, R.K.; Johnstone, M. Modeling the biomechanics of the conventional aqueous outflow pathway microstructure in the human eye. *Comput. Methods Programs Biomed.* **2022**, *221*, 106922. [[CrossRef](#)] [[PubMed](#)]
61. Grant, W.M. Further studies on facility of flow through the trabecular meshwork. *AMA Arch. Ophthalmol.* **1958**, *60*, 523–533. [[CrossRef](#)]
62. Grant, W.M. Experimental aqueous perfusion in enucleated human eyes. *Arch. Ophthalmol.* **1963**, *69*, 783–801. [[CrossRef](#)]
63. Freddo, T.F.; Johnson, M. Aqueous humor outflow resistance. *Eye’s Aqueous Humor Ed. 2* **2008**, *62*, 161–192. [[CrossRef](#)]
64. Vahabikashi, A.; Gelman, A.; Dong, B.; Gong, L.; Cha, E.D.K.; Schimmel, M.; Tamm, E.R.; Perkumas, K.; Stamer, W.D.; Sun, C.; et al. Increased stiffness and flow resistance of the inner wall of Schlemm’s canal in glaucomatous human eyes. *Proc. Natl. Acad. Sci. USA* **2019**, *116*, 26555–26563. [[CrossRef](#)]
65. Coulon, S.J.; Schuman, J.S.; Du, Y.; Bahrani Fard, M.R.; Ethier, C.R.; Stamer, W.D. A novel glaucoma approach: Stem cell regeneration of the trabecular meshwork. *Prog. Retin. Eye Res.* **2022**, *90*, 101063. [[CrossRef](#)]
66. Wang, K.; Li, G.R.; Read, A.T.; Navarro, I.; Mitra, A.K.; Stamer, W.D.; Sulchek, T.; Ethier, C.R. The relationship between outflow resistance and trabecular meshwork stiffness in mice. *Sci. Rep.* **2018**, *8*, 5848. [[CrossRef](#)]

67. McDonnell, F.; Perkumas, K.M.; Ashpole, N.E.; Kalnitsky, J.; Sherwood, J.M.; Overby, D.R.; Stamer, W.D. Shear Stress in Schlemm's Canal as a Sensor of Intraocular Pressure. *Sci. Rep.* **2020**, *10*, 5804. [[CrossRef](#)]
68. Madekurozwa, M.; Stamer, W.D.; Reina-Torres, E.; Sherwood, J.M.; Overby, D.R. The ocular pulse decreases aqueous humor outflow resistance by stimulating nitric oxide production. *Am. J. Physiol. Cell Physiol.* **2021**, *320*, C652–C665. [[CrossRef](#)]
69. Reina-Torres, E.; De Ieso, M.L.; Pasquale, L.R.; Madekurozwa, M.; van Batenburg-Sherwood, J.; Overby, D.R.; Stamer, W.D. The vital role for nitric oxide in intraocular pressure homeostasis. *Prog. Retin. Eye Res.* **2021**, *83*, 100922. [[CrossRef](#)]
70. Girkin, C.A.; Fazio, M.A.; Yang, H.; Reynaud, J.; Burgoyne, C.F.; Smith, B.; Wang, L.; Downs, J.C. Variation in the three-dimensional histomorphometry of the normal human optic nerve head with age and race: Lamina cribrosa and peripapillary scleral thickness and position. *Investig. Ophthalmol. Vis. Sci.* **2017**, *58*, 3759–3769. [[CrossRef](#)]
71. Ten Hulzen, R.D.; Johnson, D.H. Effect of fixation pressure on juxtacanalicular tissue and Schlemm's canal. *Investig. Ophthalmol. Vis. Sci.* **1996**, *37*, 114–124.
72. Burgoyne, C.F.; Downs, J.C.; Bellezza, A.J.; Hart, R.T. Three-dimensional reconstruction of normal and early glaucoma monkey optic nerve head connective tissues. *Investig. Ophthalmol. Vis. Sci.* **2004**, *45*, 4388–4399. [[CrossRef](#)]
73. Karimi, A.; Rahmati, S.M.; Grytz, R.G.; Girkin, C.A.; Downs, J.C. Modeling the biomechanics of the lamina cribrosa microstructure in the human eye. *Acta Biomater.* **2021**, *134*, 357–378. [[CrossRef](#)]
74. Overby, D.; Gong, H.; Qiu, G.; Freddo, T.F.; Johnson, M. The mechanism of increasing outflow facility during washout in the bovine eye. *Investig. Ophthalmol. Vis. Sci.* **2002**, *43*, 3455–3464.
75. Ethier, C.R.; Coloma, F.M.; Sit, A.J.; Johnson, M. Two pore types in the inner-wall endothelium of Schlemm's canal. *Investig. Ophthalmol. Vis. Sci.* **1998**, *39*, 2041–2048.
76. Karimi, A.; Razaghi, R.; Girkin, C.A.; Downs, J.C. Ocular biomechanics due to ground blast reinforcement. *Comput. Methods Programs Biomed.* **2021**, *211*, 106425. [[CrossRef](#)] [[PubMed](#)]
77. Karimi, A.; Grytz, R.; Rahmati, S.M.; Girkin, C.A.; Downs, J.C. Analysis of the effects of finite element type within a 3D biomechanical model of a human optic nerve head and posterior pole. *Comput. Methods Programs Biomed.* **2021**, *198*, 105794. [[CrossRef](#)] [[PubMed](#)]
78. Karimi, A.; Razaghi, R.; Girkin, C.A.; Downs, J.C. Ocular biomechanics during improvised explosive device blast: A computational study using eye-specific models. *Injury* **2022**, *53*, 1401–1415. [[CrossRef](#)]
79. Flocks, M. The anatomy of the trabecular meshwork as seen in tangential section. *AMA Arch. Ophthalmol.* **1956**, *56*, 708–718. [[CrossRef](#)]
80. Hogan, M.J. Histology of the human eye. An atlas and textbook. *JAMA* **1971**, *219*, 221.
81. Umihira, J.; Nagata, S.; Nohara, M.; Hanai, T.; Usuda, N.; Segawa, K. Localization of elastin in the normal and glaucomatous human trabecular meshwork. *Investig. Ophthalmol. Vis. Sci.* **1994**, *35*, 486–494.
82. Morishige, N.; Petroll, W.M.; Nishida, T.; Kenney, M.C.; Jester, J.V. Noninvasive corneal stromal collagen imaging using two-photon-generated second-harmonic signals. *J. Cataract. Refract. Surg.* **2006**, *32*, 1784–1791. [[CrossRef](#)]
83. Ammar, D.A.; Lei, T.C.; Gibson, E.A.; Kahook, M.Y. Two-photon imaging of the trabecular meshwork. *Mol. Vis.* **2010**, *16*, 935–944.
84. Hariri, S.; Johnstone, M.; Jiang, Y.; Padilla, S.; Zhou, Z.; Reif, R.; Wang, R.K. Platform to investigate aqueous outflow system structure and pressure-dependent motion using high-resolution spectral domain optical coherence tomography. *J. Biomed. Opt.* **2014**, *19*, 106013. [[CrossRef](#)]
85. Johnstone, M.A.; Hariri, S.; Jiang, Y.; Padilla, S.; Zhou, Z.H.; Wang, R.K.K. OCT Imaging Shows Collector Channels Rapidly Open & Close with Pressure Changes: A Mechanism Regulating Control of Distal Resistance? *Investig. Ophthalmol. Vis. Sci.* **2015**, *56*, 3539.
86. Park, C.Y.; Lee, J.K.; Kahook, M.Y.; Schultz, J.S.; Zhang, C.; Chuck, R.S. Revisiting ciliary muscle tendons and their connections with the trabecular meshwork by two photon excitation microscopic imaging. *Investig. Ophthalmol. Vis. Sci.* **2016**, *57*, 1096–1105. [[CrossRef](#)] [[PubMed](#)]
87. Belytschko, T.; Lu, Y.Y.; Gu, L. Element-free Galerkin methods. *Int. J. Numer. Methods Eng.* **1994**, *37*, 229–256. [[CrossRef](#)]
88. Karimi, A.; Razaghi, R.; Navidbakhsh, M.; Sera, T.; Kudo, S. Mechanical Properties of the Human Sclera Under Various Strain Rates: Elastic, Hyperelastic, and Viscoelastic Models. *J. Biomater. Tiss Eng.* **2017**, *7*, 686–695. [[CrossRef](#)]
89. Karimi, A.; Sera, T.; Kudo, S.; Navidbakhsh, M. Experimental verification of the healthy and atherosclerotic coronary arteries incompressibility via Digital Image Correlation. *Artery Res.* **2016**, *16*, 1–7. [[CrossRef](#)]
90. Pant, A.D.; Kagemann, L.; Schuman, J.S.; Sigal, I.A.; Amini, R. An imaged-based inverse finite element method to determine in-vivo mechanical properties of the human trabecular meshwork. *J. Model Ophthalmol.* **2017**, *1*, 100–111. [[CrossRef](#)] [[PubMed](#)]
91. Perkins, T.W.; Alvarado, J.A.; Polansky, J.R.; Stilwell, L.; Maglio, M.; Juster, R. Trabecular meshwork cells grown on filters. Conductivity and cytochalasin effects. *Investig. Ophthalmol. Vis. Sci.* **1988**, *29*, 1836–1846.
92. Ethier, C.R.; Kamm, R.D.; Palaszewski, B.A.; Johnson, M.C.; Richardson, T.M. Calculations of flow resistance in the juxtacanalicular meshwork. *Investig. Ophthalmol. Vis. Sci.* **1986**, *27*, 1741–1750.
93. Lepple-Wienhues, A.; Stahl, F.; Wiederholt, M. Differential smooth muscle-like contractile properties of trabecular meshwork and ciliary muscle. *Exp. Eye Res.* **1991**, *53*, 33–38. [[CrossRef](#)]
94. Souli, M. ALE incompressible fluid in LS-DYNA. In Proceedings of the 11th International LS-DYNA Conference, Detroit, MI, USA, 6–8 June 2010; pp. 29–36.
95. Aquelet, N.; Souli, M. ALE Incompressible Fluid in LS-DYNA<sup>®</sup>. *FSI/ALE* **2012**, *21*, 6.

96. Peery, J.S.; Carroll, D.E. Multi-Material ALE methods in unstructured grids. *Comput. Methods Appl. Mech. Eng.* **2000**, *187*, 591–619. [[CrossRef](#)]
97. Aquelet, N. ALE adaptive mesh refinement in LS-Dyna. In Proceedings of the 12th International LS-DYNA Users Conference, Detroit, MI, USA, 3–5 June 2012.
98. Razaghi, R.; Biglari, H.; Karimi, A. Risk of rupture of the cerebral aneurysm in relation to traumatic brain injury using a patient-specific fluid-structure interaction model. *Comput. Methods Programs Biomed.* **2019**, *176*, 9–16. [[CrossRef](#)] [[PubMed](#)]
99. Vass, C.; Hirn, C.; Unger, E.; Mayr, W.; Georgopoulos, M.; Rainer, G.; Richter-Maksch, S. Human aqueous humor viscosity in cataract, primary open angle glaucoma and pseudoexfoliation syndrome. *Investig. Ophthalmol. Vis. Sci.* **2004**, *45*, 5030.
100. Coleman, D.J.; Trokel, S. Direct-recorded intraocular pressure variations in a human subject. *Arch. Ophthalmol.* **1969**, *82*, 637–640. [[CrossRef](#)] [[PubMed](#)]
101. Erickson-Lamy, K.; Rohen, J.W.; Grant, W.M. Outflow facility studies in the perfused bovine aqueous outflow pathways. *Curr. Eye Res.* **1988**, *7*, 799–807. [[CrossRef](#)] [[PubMed](#)]
102. Erickson-Lamy, K.; Rohen, J.W.; Grant, W.M. Outflow facility studies in the perfused human ocular anterior segment. *Exp. Eye Res.* **1991**, *52*, 723–731. [[CrossRef](#)]
103. Wiederholt, M.; Bielka, S.; Schweig, F.; Lutjen-Drecoll, E.; Lepple-Wienhues, A. Regulation of outflow rate and resistance in the perfused anterior segment of the bovine eye. *Exp. Eye Res.* **1995**, *61*, 223–234. [[CrossRef](#)]
104. Ramos, R.F.; Sumida, G.M.; Stamer, W.D. Cyclic mechanical stress and trabecular meshwork cell contractility. *Investig. Ophthalmol. Vis. Sci.* **2009**, *50*, 3826–3832. [[CrossRef](#)]
105. Sherwood, J.M.; Reina-Torres, E.; Bertrand, J.A.; Rowe, B.; Overby, D.R. Measurement of Outflow Facility Using iPerfusion. *PLoS ONE* **2016**, *11*, e0150694. [[CrossRef](#)]
106. Yuan, F.; Schieber, A.T.; Camras, L.J.; Harasymowycz, P.J.; Herndon, L.W.; Allingham, R.R. Mathematical Modeling of Outflow Facility Increase With Trabecular Meshwork Bypass and Schlemm Canal Dilatation. *J. Glaucoma* **2016**, *25*, 355–364. [[CrossRef](#)]
107. Szopos, M.; Cassani, S.; Guidoboni, G.; Prud'Homme, C.; Sacco, R.; Siesky, B.; Harris, A. Mathematical modeling of aqueous humor flow and intraocular pressure under uncertainty: Towards individualized glaucoma management. *J. Model. Ophthalmol.* **2016**, *2*, 29–39. [[CrossRef](#)]
108. Sherwood, J.M.; Stamer, W.D.; Overby, D.R. A model of the oscillatory mechanical forces in the conventional outflow pathway. *J. R. Soc. Interface* **2019**, *16*, 20180652. [[CrossRef](#)] [[PubMed](#)]
109. Tripathi, R. Tracing the bulk outflow route of cerebrospinal fluid by transmission and scanning electron microscopy. *Brain Res.* **1974**, *80*, 503–506. [[CrossRef](#)]
110. Gong, H.; Tripathi, R.C.; Tripathi, B.J. Morphology of the aqueous outflow pathway. *Microsc. Res. Tech.* **1996**, *33*, 336–367. [[CrossRef](#)]
111. Johnson, M. Mechanisms and routes of aqueous humor drainage. *Princ. Pract. Ophthalmol.* **2000**, *1*, 2577–2595.
112. Ethier, C.R. The inner wall of Schlemm's canal. *Exp. Eye Res.* **2002**, *74*, 161–172. [[CrossRef](#)]
113. Tamm, E.R.; Braunger, B.M.; Fuchshofer, R. Intraocular Pressure and the Mechanisms Involved in Resistance of the Aqueous Humor Flow in the Trabecular Meshwork Outflow Pathways. *Prog. Mol. Biol. Transl. Sci.* **2015**, *134*, 301–314. [[CrossRef](#)]
114. Acott, T.S.; Vranka, J.A.; Keller, K.E.; Raghunathan, V.; Kelley, M.J. Normal and glaucomatous outflow regulation. *Prog. Retin. Eye Res.* **2021**, *82*, 100897. [[CrossRef](#)]
115. McDowell, C.M.; Kizhatil, K.; Elliott, M.H.; Overby, D.R.; van Batenburg-Sherwood, J.; Millar, J.C.; Kuehn, M.H.; Zode, G.; Acott, T.S.; Anderson, M.G.; et al. Consensus Recommendation for Mouse Models of Ocular Hypertension to Study Aqueous Humor Outflow and Its Mechanisms. *Investig. Ophthalmol. Vis. Sci.* **2022**, *63*, 12. [[CrossRef](#)]
116. Vranka, J.A.; Acott, T.S. Pressure-induced expression changes in segmental flow regions of the human trabecular meshwork. *Exp. Eye Res.* **2017**, *158*, 67–72. [[CrossRef](#)]
117. Borrás, T.; Rowlette, L.L.; Tamm, E.R.; Gottanka, J.; Epstein, D.L. Effects of elevated intraocular pressure on outflow facility and TIGR/MYOC expression in perfused human anterior segments. *Investig. Ophthalmol. Vis. Sci.* **2002**, *43*, 33–40.
118. Lakes, R.; Lakes, R.S. *Viscoelastic Materials*; Cambridge University Press: Cambridge, UK, 2009.
119. Gould, T.E.; Jesunathadas, M.; Nazarenko, S.; Piland, S.G. Mouth Protection in Sports. In *Materials in Sports Equipment*; Subic, A., Ed.; Woodhead Publishing: Sawston, UK, 2019; pp. 199–231.
120. Malkin, A.Y. The state of the art in the rheology of polymers: Achievements and challenges. *Polym. Sci. Ser. A* **2009**, *51*, 80–102. [[CrossRef](#)]
121. Ubaidillah; Sutrisno, J.; Purwanto, A.; Mazlan, S.A. Recent Progress on Magnetorheological Solids: Materials, Fabrication, Testing, and Applications. *Adv. Eng. Mater.* **2015**, *17*, 563–597. [[CrossRef](#)]
122. Chatzigeorgiou, G.; Charalambakis, N.; Chemisky, Y.; Meraghni, F. Continuum Mechanics and Constitutive Laws. In *Thermo-mechanical Behavior of Dissipative Composite Materials*; Chatzigeorgiou, G., Charalambakis, N., Chemisky, Y., Meraghni, F., Eds.; Elsevier: Amsterdam, The Netherlands, 2017; pp. 37–87.
123. Grierson, I.; Lee, W. Changes in the monkey outflow apparatus at graded levels of intraocular pressure: A qualitative analysis by light microscopy and scanning electron microscopy. *Exp. Eye Res.* **1974**, *19*, 21–33. [[CrossRef](#)]
124. Van Buskirk, E.M. Anatomic correlates of changing aqueous outflow facility in excised human eyes. *Investig. Ophthalmol. Vis. Sci.* **1982**, *22*, 625–632.

125. Ethier, C.R.; Read, A.T.; Chan, D. Biomechanics of Schlemm's canal endothelial cells: Influence on F-actin architecture. *Biophys. J.* **2004**, *87*, 2828–2837. [[CrossRef](#)]
126. Stamer, W.D.; Lei, Y.; Boussommier-Calleja, A.; Overby, D.R.; Ethier, C.R. eNOS, a pressure-dependent regulator of intraocular pressure. *Investig. Ophthalmol. Vis. Sci.* **2011**, *52*, 9438–9444. [[CrossRef](#)]
127. Rosenquist, R.; Epstein, D.; Melamed, S.; Johnson, M.; Grant, W.M. Outflow resistance of enucleated human eyes at two different perfusion pressures and different extents of trabeculotomy. *Curr. Eye Res.* **1989**, *8*, 1233–1240. [[CrossRef](#)]
128. Maepea, O.; Bill, A. Pressures in the juxtacanalicular tissue and Schlemm's canal in monkeys. *Exp. Eye Res.* **1992**, *54*, 879–883. [[CrossRef](#)]
129. Schuman, J.S.; Chang, W.; Wang, N.; de Kater, A.W.; Allingham, R.R. Excimer laser effects on outflow facility and outflow pathway morphology. *Investig. Ophthalmol. Vis. Sci.* **1999**, *40*, 1676–1680.
130. McDonnell, F.; Dismuke, W.M.; Overby, D.R.; Stamer, W.D. Pharmacological regulation of outflow resistance distal to Schlemm's canal. *Am. J. Physiol. Cell Physiol.* **2018**, *315*, C44–C51. [[CrossRef](#)]
131. Acott, T.S.; Kelley, M.J. Extracellular matrix in the trabecular meshwork. *Exp. Eye Res.* **2008**, *86*, 543–561. [[CrossRef](#)] [[PubMed](#)]
132. Acott, T.S.; Kelley, M.J.; Keller, K.E.; Vranka, J.A.; Abu-Hassan, D.W.; Li, X.; Aga, M.; Bradley, J.M. Intraocular pressure homeostasis: Maintaining balance in a high-pressure environment. *J. Ocul. Pharm.* **2014**, *30*, 94–101. [[CrossRef](#)]
133. Sit, A.J.; Coloma, F.M.; Ethier, C.R.; Johnson, M. Factors affecting the pores of the inner wall endothelium of Schlemm's canal. *Investig. Ophthalmol. Vis. Sci.* **1997**, *38*, 1517–1525.
134. Swain, D.L.; Le, T.D.; Yasmin, S.; Fernandes, B.; Lamaj, G.; Dasgupta, I.; Gao, Y.; Gong, H. Morphological factors associated with giant vacuoles with I-pores in Schlemm's canal endothelial cells of human eyes: A serial block-face scanning electron microscopy study. *Exp. Eye Res.* **2021**, *205*, 108488. [[CrossRef](#)] [[PubMed](#)]
135. Johnstone, M.; Xin, C.; Acott, T.; Vranka, J.; Wen, J.; Martin, E.; Wang, R.K. Valve-Like Outflow System Behavior With Motion Slowing in Glaucoma Eyes: Findings Using a Minimally Invasive Glaucoma Surgery-MIGS-Like Platform and Optical Coherence Tomography Imaging. *Front. Med.* **2022**, *9*, 815866. [[CrossRef](#)]
136. Martin, E.A.; Johnstone, M.A. A Novel Technique Identifies Valve-Like Pathways Entering and Exiting Schlemm's Canal in *Macaca nemestrina* Primates With Similarities to Human Pathways. *Front. Cell. Dev. Biol.* **2022**, *10*, 868029. [[CrossRef](#)]